Supporting Information

for

Aromaticity and antiaromaticity in a molecular nanoring

Martin D. Peeks, Timothy D. W. Claridge, Harry L. Anderson

Notes on terminology

Diatropic and paratropic: a "diatropic current" indicates an aromatic system, and a "paratropic current" an antiaromatic system. The terms "diatropic" and "paratropic" relate to the direction of the induced ring current around the conjugated aromatic system, as described in the main text.

Experimental section

All porphyrin compounds were synthesised as described previously[S1]. Bulky 3,5-bis(trihexylsilyl)phenyl solubilising sidegroups were chosen to permit high-concentration NMR experiments, and to inhibit aggregation. ***c*-P6·T6** was synthesised from 200 mg of monomer ***l*-P1** and small amounts of larger rings (***c*-P8** to ***c*-P16**) were isolated as side products, characterised by gel permeation chromatography (GPC), NMR, MALDI-TOF MS and UV-Vis-NIR spectroscopy.

Oxidation experiments used the hexafluoroantimonate salts of diacetylferrocenium (diAcFc, E_{red} = 0.50 V *vs*. Fc/Fc^+), tris(4-bromophenyl)aminium ($BAHA_F$, E_{red} = 0.70 V *vs*. Fc/Fc^+), thianthrenium (Thn, E_{red} = 0.86 V *vs*. Fc/Fc^+) and tris(2,4-dibromophenyl)aminium ($DIBAHA_F$, E_{red} = 1.14 V *vs*. Fc/Fc^+), and also silver hexafluoroantimonate with iodine (E_{red} > 1.14 V *vs*. Fc/Fc^+) (SI Fig. S1)[S2]. All oxidation experiments were conducted in J. Young tap NMR tubes using CD_2Cl_2 stored over molecular sieves, using standard Schlenk line techniques. For titrations, a solution of oxidant (40–50 mM) was added to a solution of porphyrin compound (*ca.* 4 mg/mL) in the NMR tube, cooled to –78 °C and kept under a flow of argon. For single point oxidations, an excess of an oxidant as a solution or suspension was added to the porphyrin solution in the same manner. Tubes were then closed and quickly transferred to an NMR spectrometer pre-cooled to the appropriate temperature. Exposure to water is immediately deleterious to porphyrin polycations, but they are stable to oxygen (O_2). The use of rubber subaseals was avoided: we found that the introduction of small quantities of rubber (even by non-coring needles) has an immediate quenching effect on the cations.

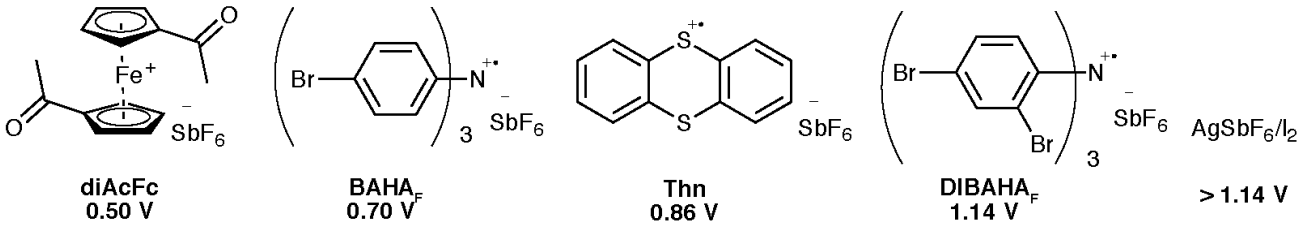

Fig. S1: Chemical structures of oxidants used in this study. Abbreviations are expanded in the text. The potentials underneath each structure refer to the E_{red} for the first reduction of each oxidant.

NMR measurements were performed on a Bruker AVII 500 (5 mm TXI probe) or a Bruker AVIII 700 (5 mm TCI cryoprobe). Chemical shifts are reported in ppm *vs.* the residual solvent peak. The ^{1}H NMR spectra of ***c*-P6·T6^{4+}** and ***c*-P6·T6^{6+}** are unchanged on warming from 213 K to 278 K. In contrast, the spectrum of ***c*-P6·T6^{12+}** broadens upon warming, and this change becomes irreversible if the sample is kept at 20 °C for more than a few minutes, due to decomposition. Neutral ***c*-P6·T6** is insoluble in CD_2Cl_2 at low temperatures (<233 K), but solubility improves upon oxidation. The ^{1}H NMR spectra of all species are field-independent, from 500 MHz (11.7 T) to 700 MHz (16.4 T).

Voltammetric measurements were made using an Autolab PGSTAT 12 with a glassy-carbon working electrode, platinum wire counter electrode and Ag/AgCl quasi-reference electrode. Voltammograms

were referenced to the Fc/Fc^+ couple (0.0 V) as an internal reference after each measurement. Square wave voltammograms were acquired with a 5 mV step potential, 50 mV modulation amplitude and 5 Hz frequency. Exclusion of water was essential for the acquisition of clean voltammograms. The supporting electrolyte salt (tetra-*n*-butylammonium hexafluorophosphate, TBAP) was dried by melting *in vacuo*. CH_2Cl_2 (dried over alumina (MBraun SPS), distilled from CaH_2, and stored over 4 Å molecular sieves) was added to the dry electrolyte to a concentration of 0.1 M electrolyte. Analyte solutions were prepared by addition of this electrolyte solution to porphyrin oligomer (2–10 mg), and measurements were performed over 4 Å molecular sieves.

Spectroelectrochemistry measurements used an optically transparent thin layer electrochemical (OTTLE) cell comprising a three-electrode system sandwiched between two CaF_2 optical windows, with a ~200 μm path length. The working and auxiliary electrodes were platinum gauzes, and the quasi-reference electrode was a silver wire. NIR spectra were recorded using a Bruker Vertex 80, and IR spectra using a Bruker Tensor 27. Cyclic voltammograms were measured using a Palmsens EmStat3+ with scan rates of 10 mV/s and 5 mV/s for the NIR and IR measurements, respectively.

Details of computational chemistry methods

DFT calculations were all performed using a model of ***c*-P6** in which solubilising aryl groups had been removed (D_{6h} initial symmetry). Geometries were optimised using Gaussian09/D.01[S3] and the B3LYP/6-31G* functional/basis set combination[S4-S6]. The neutral and 6+ rings converged to D_{6h} symmetry, while the 4+ and 12+ rings lost symmetry (C_1). The 2+ ring was optimised with both unrestricted and restricted DFT, and the stability of triplet and singlet wavefunctions were checked in the former case. The 2+ oxidation state optimised to C_{2h} symmetry and a singlet ground state with spin contamination $\langle S^2 \rangle = 0.7342$ (0.2022 after annihilation). The converged geometry optimised structures were confirmed as minima by performing frequency calculations, which showed no imaginary frequencies. NICS/susceptibility and ACID calculations were conducted using the GIAO and CSGT methods, respectively, as implemented in Gaussian09/D.01. NICS grids were calculated with 1 Å resolution on a 20 × 20 Å grid. Version 2.0 of the ACID program[S7] (external to Gaussian) was used to generate the ACID results, and they were visualised using POV-Ray. Application of Grimme's D3 dispersion correction[S8] to geometry optimisations did not affect the conclusions of subsequent NICS calculations. The D3 correction caused small changes in the geometries (RMSD 0.018–0.025 Å) and this affected the NICS by 0–5% of their B3LYP values. The M06-2X and ωB97X-D functionals[S9,S10] were tested on the 0+, 4+, 6+ and 12+ oxidation states and gave similar NICS values to B3LYP (Table S5). M06-2X is a highly parameterised hybrid meta GGA (generalised gradient approximation) functional with good performance for main group thermochemistry and non-covalent interactions. ωB97X-D is a long-range corrected hybrid GGA functional with an empirical dispersion correction term, and similar areas of applicability as M06-2X with the addition of good treatment of the self-interaction error. The magnitude of NICS(0) for the antiaromatic 4+ oxidation state decreases according to B3LYP > M06-2X > ωB97X-D due to a corresponding increase in ellipticity (f = 0.049, 0.088 and 0.166 for B3LYP, M06-2X and ωB97X-D, respectively). For ωB97X-D, this elliptical distortion results in predicted non-aromaticity of the 4+ state. The presence of template (**T6**) in the experimental studies maintains an approximately circular geometry by limiting such distortion, promoting antiaromaticity.

Processing software

NMR spectra were processed using TopSpin v 3.0. EXSY data were fit using the Curve Fitting Tool in MATLAB and errors were propagated with the help of the Python (3.5) uncertainties package. Figures were composed in Adobe Illustrator and Inkscape. Spectroelectrochemical and NICS surface plots were generated using MATLAB. Molecular orbitals were visualised using Chimera.

The interporphyrin torsion barriers in *c*-P6^{6+} and *c*-P6^{12+}

In template-free neutral ***c*-P6**, the barrier to inter-porphyrin torsion about the butadiyne linkers is likely to be similar to that in ***l*-P2**, *ca.* 2.1 kJ mol^{-1},[S11] thus the porphyrins are rapidly rotating at room temperature (k_BT = 2.5 kJ mol^{-1}). Consequently, only one resonance is observed in ^{1}H NMR for the *o* and *o′* (ortho) protons in fast exchange. No broadening is apparent when reducing temperature to 223 K in CD_2Cl_2, below which solubility becomes limiting. In contrast, the *o*/*o′* resonances in oxidised nanorings ***c*-P6^{6+}** and ***c*-P6^{12+}** are in slow exchange at 223 K.

VT NMR can be used to determine the coalescence temperature T_c between the *o* and *o′* resonances and hence the exchange activation barrier at T_c (*via* the Eyring equation). Estimates of T_c from VT NMR are >278 K and ~233 K for 6+ and 12+, respectively. Estimation of T_c is confounded by broadening of the entire spectrum of oxidised species at elevated temperatures, perhaps owing to paramagnetic exchange with residual oxidant. To avoid this problem, we used 2D-EXSY NMR to measure the exchange rate constant *k* at 213 K for ***c*-P6^{6+}** and ***c*-P6^{12+}**.

A phase-sensitive NOESY (EXSY) pulse sequence with gradient enhancement (noesygpph) was employed with variable mixing times t_{mix} from 5 ms to 125 ms. The recycle delay (*d1*) was 1 s. The Fourier-transformed (with a squared sine bell window function applied to the FID) spectra were phase-corrected and a 2D baseline of 5th order was subtracted. The intensities of peaks of interest were determined by volume integration.

The pertinent *o*/*o′* exchange was modelled as a simple two-spin system, with spins labelled *A* and *B*. An equal population of sites *A* and *B* was assumed, leading to the following equalities for the intensities *I* of on-diagonal peaks (I_{AA} and I_{BB}) and off-diagonal crosspeaks (I_{AB} and I_{BA})[S12,S13]. These equalities are not experimental facts due to spectral overlap, but this does not affect the analysis.

$$I_{AA} = I_{BB}$$

$$I_{AB} = I_{BA}$$

The intensities *I* can be defined as follows:

$$I_{AA} = \frac{1}{4} e^{\frac{-t_{mix}}{T_1}} [1 + e^{-k\,t_{mix}}] M^0$$

$$I_{AB} = \frac{1}{4} e^{\frac{-t_{mix}}{T_1}} [1 - e^{-k\,t_{mix}}] M^0$$

Where t_{mix} is exchange mixing time, T_1 is the spin-lattice relaxation time (assumed equal for *A* and *B*), *k* is the exchange rate constant and M^0 is the initial magnetisation. If we take the ratio of intensities *r*, the equations simplify, removing the dependencies on M^0 and T_1:

$$r = \frac{I_{AB} + I_{BA}}{I_{AA} + I_{BB}}$$

$$r = \frac{1 - e^{-k\,t_{mix}}}{1 + e^{-k\,t_{mix}}}$$

The experimental data points and fit for 6+ and 12+ are shown in SI Figs S2 and S3 respectively.

The equations for I_{AA} and I_{AB} are based on the following chemical system:

$$\mathrm{A} \underset{k_{BA}}{\overset{k_{AB}}{\rightleftharpoons}} \mathrm{B}$$

which, given the equal populations of *A* and *B*, leads to the following definition of *k*.[S12]

$$p_A = p_B = 0.5$$

$$k_{AB} = p_B\,k \qquad k_{BA} = p_A\,k$$

$$k = 2k_{AB} = 2k_{BA} = k_{AB} + k_{BA}$$

In 1992, Green *et al.* noted that a multiplicative factor of two must be applied to k_{obs} (= k_{AB}) determined by magnetisation transfer experiments for equally populated two-site exchange in order to deliver a k_{chem} suitable for the calculation of $\Delta G^{\ddagger}$.[S14] The rationale is that a species at the midpoint of a symmetric reaction profile will only decay in such a way that gives rise to magnetisation transfer 50% of the time. This notion is the direct analogue of the transmission coefficient κ in the Eyring equation:

$$k = \kappa \frac{k_B T}{h} \exp(-\frac{\Delta G^{\ddagger}}{RT})$$

In words, if we denote labelling with an asterisk, the species A^*B will form a transition state in which the label is no longer well-defined: $[AB]^*$. This transition state can decay with 50% probability (owing to the symmetric nature of the reaction profile) to give A^*B and AB^*. A rate constant k_{AB} only describes those transition states which result in magnetisation transfer from *A* to *B*, thus a value of $\kappa = 0.5$ must be used, analogous to Green's multiplicative factor of two for k_{chem} (*i.e.*, $k_{chem} = 2\,k_{obs} = k_{AB} / \kappa$).

In our case the formulations of *k*, I_{AA} and I_{AB} give us k_{chem} directly[S12], such that we use a transmission coefficient $\kappa = 1$ to determine $\Delta G^{\ddagger}$. The results are shown in Table S1.

The chemical exchange rate constant at the coalescence temperature (T_c) can be determined by taking an estimate for $\Delta\nu$ between *o*/*o'* in slow exchange from the templated nanoring spectra (Tables S2 and S3), and thus T_c can be estimated using $\Delta G^{\ddagger}$ from the above analysis. The quantitative analysis of errors in this EXSY experiment is difficult – rather than relying on the 95% confidence interval of the fit (0.07 s^{-1} and 35 s^{-1} for 6+ and 12+, respectively), we have adopted an empirical error of 25%.

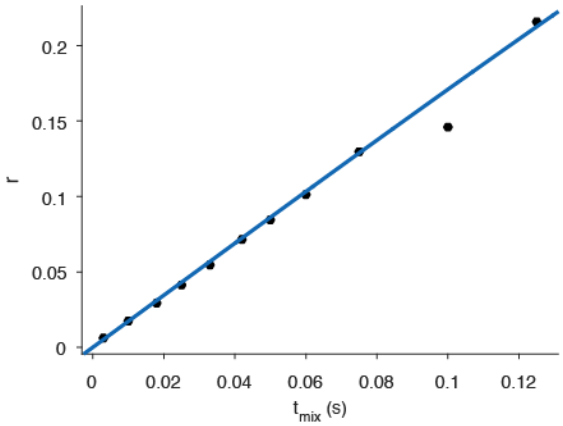

Fig. S2: Fit of ^{1}H EXSY data (500 MHz, CD_2Cl_2, 213 K) for *o*/*o′* exchange in ***c*-P6^{6+}** as a function of t_{mix}.

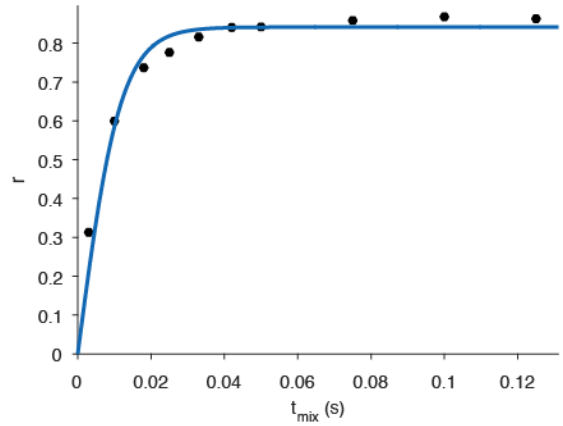

Fig. S3: Fit of ^{1}H EXSY data (500 MHz, CD_2Cl_2, 213 K) for *o*/*o′* exchange in ***c*-P6^{12+}** as a function of t_{mix}. A normalisation factor was used in this fit, equal to 0.84.

Table S1: Kinetic parameters for porphyrin torsional rotation in ***c*-P6^{6+}** and ***c*-P6^{12+}** from ^{1}H EXSY measurements (500 MHz, CD_2Cl_2, 213 K).

	$k_{213\,K}$ (s^{-1})	$\Delta G^{\ddagger}_{213\,K}$ (kJ mol^{-1})	$k_{chem,Tc}$ (s^{-1})	T_c (K)
***c*-P6^{6+}**	3.45 ± 0.86	49.48 ± 0.44	4154	282 ± 2
***c*-P6^{12+}**	172 ± 43	42.56 ± 0.44	1644	234 ± 2

Based on the absence of exchange broadening in neutral ***c*-P6** at 223 K (hence T_c << 223 K, and k_{ex} = 578 s^{-1} at T_c), an upper bound of $\Delta G^{\ddagger}$ << 42.3 kJmol^{-1} can be assigned for the neutral oxidation state.

The value of the exchange rate constant *k* at 213 K for ***c*-P6^{6+}** is of the same order as that measured for *o*/*o′* exchange due to aryl rotation about the *meso*–aryl bond in a similar complex (a templated [10]-porphyrin nanoring), at 298 K: 4 s^{-1} and 0.4 s^{-1} for two inequivalent porphyrin sites[S15]. These values of *k* correspond to $\Delta G^{\ddagger}$ of 70 kJ mol^{-1} and 263 kJ mol^{-1}, respectively, and are thus unlikely to contribute to the EXSY spectra at 213 K. Furthermore, no *o*/*o′* exchange is observed in the 223 K NOESY spectra of ***c*-P6·T6^{6+}** and ***c*-P6·T6^{12+}** with t_{mix} = 250 ms.

Paramagnetic susceptibility by Evans' Method

We applied the principles of Evans' method[S16-19] for the determination of magnetic susceptibility by NMR to determine the approximate magnetic susceptibilities of the [6]-porphyrin nanoring oxidation states. At the outset, we expected to observe increases in paramagnetic susceptibility for the *odd* oxidation states (1+, 3+, 5+) and for the free oxidant, with near-zero relative magnetic susceptibility for the closed-shell oxidation states.

The Evans' method involves separating an analyte and a reference solution by placing one in an isolated coaxial chamber within the other. In our case, we placed a flame-sealed capillary of $CFCl_3$ in d_8-toluene into a standard 4 mm J. Young NMR tube containing the analyte solution, $CFCl_3$ and CD_2Cl_2. The reference capillary was supported with custom-made PTFE spacers. With this assembly, we were able to conduct titrations of oxidant into ***c*-P6·T6** solutions, and measure the frequency shift between the $CFCl_3$ resonances in the ^{19}F domain. We chose to use $CFCl_3$ since the ^1H domain was too crowded to permit reliable measurement of a chemical shift difference between analyte and reference probe resonances for the commonly used references. However, the ^{19}F resonance for $CFCl_3$ is split into a complicated multiplet pattern owing to different isotopic chemical shift effects from $^{35/37}Cl$ (the resonance resembles the mass spectrum isotope pattern for $CFCl_3$, Fig. S4B). For this reason, we use d_8-toluene as the solvent in our reference capillary, to provide an appreciable initial frequency difference between analyte and reference chamber $CFCl_3$ resonances, and make subsequent measurements of $\Delta\nu$ (calculated relative to to the $\Delta\nu$ between $CFCl_3$ resonances in the reference and analyte compartments in otherwise pure solvent (without ***c*-P6·T6**)) more reliable.

Attempts to use Evans' method without an explicit reference compound, instead monitoring the ^2H solvent resonances, failed due to the broad line-width and low signal to noise of the ^2H spectrum. Control experiments indicated that, in the absence of analyte, $\Delta\nu$ with $CFCl_3$ varied by about 1 Hz/K temperature variation. In the context of a titration, this implies an error of at least ±2 Hz in each $\Delta\nu$.

A titration of $DIBAHA_F$ (*ca.* 44.5 mM, in 21 μL increments) into ***c*-P6·T6** (*ca.* 2.0 mM, 450 μL in CD_2Cl_2) was conducted at 243 K. At this concentration and field, one equivalent of oxidant (2.0 mM, *i.e.* 2.0×10^{-6} mol cm^{-3}) with a magnetic moment of 1 μ_B (Bohr magneton) would give an imperceptible (1–2 Hz) frequency difference $\Delta\nu$. However, our experimental results (Figure S4) show a huge $\Delta\nu$ (66 Hz) for the antiaromatic tetracation ***c*-P6·T6^{4+}**. This surprising result corresponds to a large paramagnetic susceptibility and is supported by DFT calculations for ***c*-P6** (SI Fig. S4 and Table S2).

The magnetic susceptibility χ_{mol} is related to the chemical shift difference $\Delta\nu$ by:

$$\chi_{mol} = -\frac{3\Delta\nu}{4\pi\nu_0 c}$$

Where ν_0 is the spectrometer frequency (470 MHz) and c is the concentration of ***c*-P6**, in mol cm^{-3}. A diamagnetic solvent correction has been neglected from this analysis.

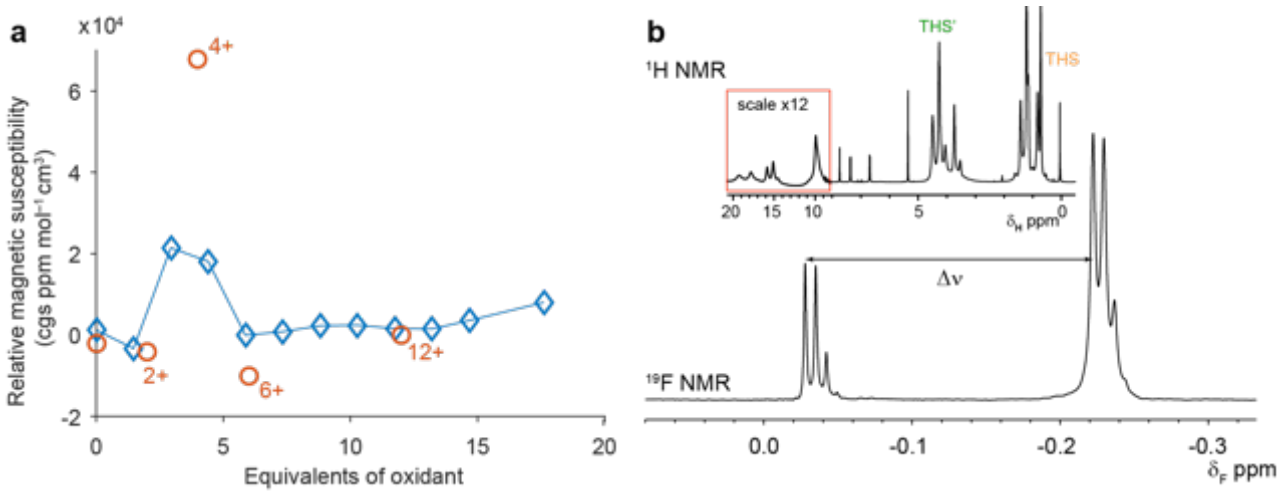

Fig S4: (a) Experimental magnetic susceptibility during an NMR (243 K, 470 MHz (^{19}F)) titration of DIBAHA$_F$ into ***c*-P6·T6** in CD_2Cl_2 (blue diamonds). The molar susceptibility was calculated based on the approximate concentration of ***c*-P6·T6**, and the concentration of oxidant has been corrected by a factor of 1.3 to account for error in the concentrations of oxidant and porphyrin. The red points show the DFT (B3LYP/6-31G*) calculated magnetic susceptibility. (b) Example ^{19}F (470 MHz) NMR spectrum showing the measurement of Δν, and the corresponding ^{1}H (500 MHz) spectrum, inset. These spectra correspond to the third data point (~4 eq. oxidant) in (a).

Supplementary Tables

Table S2: Calculated (NICS, ppm) and experimental ($\Delta\delta$, ppm) parameters for the description of aromaticity in different oxidation states of ***c*-P6** (calculations were performed on a ***c*-P6** model). Negative NICS/$\Delta\delta$ values correspond to aromaticity, and positive NICS/$\Delta\delta$ values to antiaromaticity. The NICS(0) values were calculated at the centre of the ring. The NICS and magnetic susceptibility for the dication were calculated using unrestricted DFT.

	0+	**2+**	**4+**	**6+**	**12+**
$n\ \pi\ e^-$	84	82	80	78	72
Hückel classification	$4n\ \pi$	$4n + 2\ \pi$	$4n\ \pi$	$4n + 2\ \pi$	$4n\ \pi$
$NICS(0)_{zz}$ (ppm)	1	–10	304	–41	1
$NICS(0)_{iso}$ (ppm)	–1	–5	101	–13	1
χ_{mol} $cm^3\ mol^{-1}$ (cgs)	-2.0×10^{-3}	-4.2×10^{-3}	6.8×10^{-2}	-1.0×10^{-2}	1.1×10^{-4}
$\Delta\delta_{o,o'}$ (ppm)	0.26	—	—	–1.87	–0.74
$\Delta\delta_{THS,THS'}$ (ppm)	0.14	—	3.45	–0.70	–0.18

Table S3: ^1H and ^{13}C NMR chemical shifts for ***c*-P6·T6**, ***c*-P6·T6**$^{4+}$, ***c*-P6·T6**$^{6+}$ and ***c*-P6·T6**$^{12+}$. "THS CH_3" refers to the terminal methyl in the hexyl chain of the trihexylsilyl group (determined by multiplicity edited HSQC), and "THS CH_2" refers to the methylene proximal (α) to the silicon atom, determined by chemical shift. The inner and outer THS(′) manifolds could be readily distinguished by COSY, TOCSY and NOESY. All chemical shifts are given in ppm.

	Neutral		**4+**		**6+**		**12+**	
	^{1}**H**	^{13}**C**	^{1}**H**	^{13}**C**	^{1}**H**	^{13}**C**	^{1}**H**	^{13}**C**
α	2.41	143.4	—	—	5.71	145.9	11.31	151.0
β	4.99	119.9	—	—	5.27	—	8.83	125.6
γ	5.45	124.3	—	—	~5.17	—	7.94	126.3
δ	5.56	131.2	—	—	~5.17	—	7.73	131.8
a	9.56	130.6	—	—	6.52	128.2	6.05	133.6
b	8.75	133.3	—	—	5.99	133.4	5.77	136.5
o	8.06	141.6	—	—	7.78	—	7.31	128.2
o′	8.32	140.8	—	—	5.91	—	6.57	134.4
p	8.02	139.9	—	—	7.92	—	7.58	144.6
THS CH_3	0.77	14.4	0.69	13.9	0.84	14.2	0.83	13.7
THS′ CH_3	0.91	14.4	4.14	17.3	0.14	13.6	0.65	14.1
THS CH_2	0.92	13.0	0.80	11.7	0.73	11.6	0.75	~13
THS′ CH_2	0.92	13.0	4.73	14.9	0	10.8	0.59	~13
$\Delta\delta_{o,o'}$	0.26	–0.8	—	—	–1.87	—	–0.74	6.2
$\Delta\delta_{THS,THS'\ CH3}$	0.14	0	3.45	3.4	–0.70	–0.6	–0.18	0.4
$\Delta\delta_{THS,THS'\ CH2}$	0	0	3.93	3.2	–0.73	–0.8	–0.16	~0

Table S4: Chemical shift differences ($\Delta\delta_{X+} = \Delta\delta_{\mathbf{T6},\ free} - \Delta\delta_{\mathbf{T6}\ in\ [c\text{-}P6\cdot T6]X+}$) for the template protons (α, β, γ and δ) in ***c*-P6·T6**, ***c*-P6·T6**$^{6+}$ and ***c*-P6·T6**$^{12+}$, *vs.* unbound template (**T6**, 400 MHz, $CDCl_3$). All values are given in ppm.

	T6	$\Delta\delta_0$	$\Delta\delta_{6+}$	$\Delta\delta_{12+}$
α	8.54	6.13	2.83	–2.77
β	7.33	2.34	2.06	–1.50
γ	7.24	1.79	2.07	–0.70
Δ	7.02	1.46	1.85	–0.71

Table S5: NICS(0)$_{iso}$ and (in brackets) NICS(0)$_{zz}$ values (ppm) for ***c*-P6** in different oxidation states, caculated using different DFT functionals. The 6-31G* basis set was used throughout. The NICS(0) values were calculated at the centre of the ring.

	0+	**2+**	**4+**	**6+**	**12+**
B3LYP//B3LYP	–1 (1)	–5 (–10)	101 (304)	–13 (–41)	1 (1)
B3LYP//B3LYP-D3	–1 (1)	–5 (–9)	106 (320)	–13 (–41)	1 (1)
M06-2X//M06-2X	–2 (1)	n.d.	3 (12)	–15 (–45)	0 (1)
ωB97X//ωB97X-D	–2 (1)	n.d.	0 (1)	–16 (–46)	0 (1)

Supplementary Figures

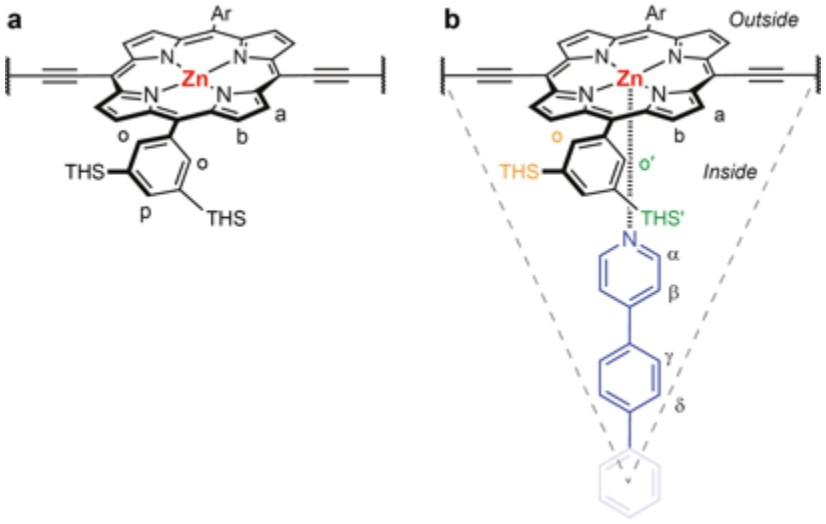

Fig. S5: NMR assignment labels used for (a) linear oligomers and (b) ***c*-P6·T6.**

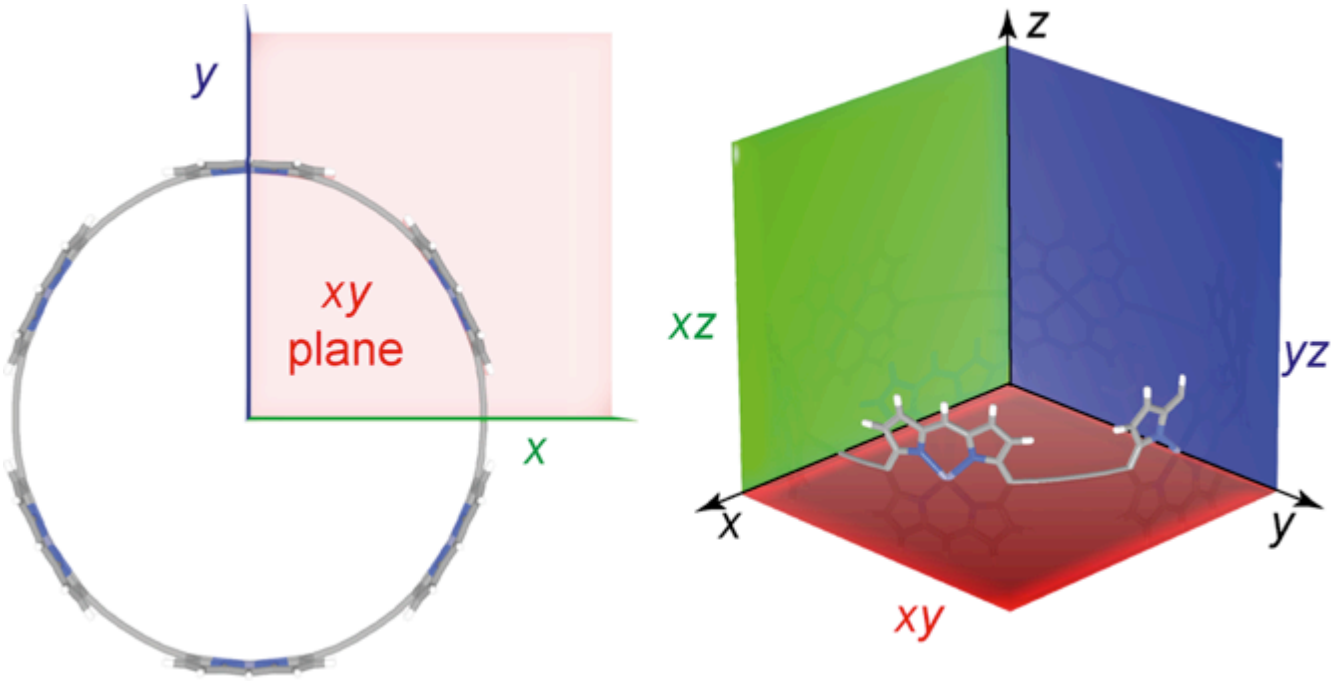

Fig. S6: Representations of ***c*-P6** describing the *xy*, *xz* and *yz* planes in which NICS grids have been calculated.

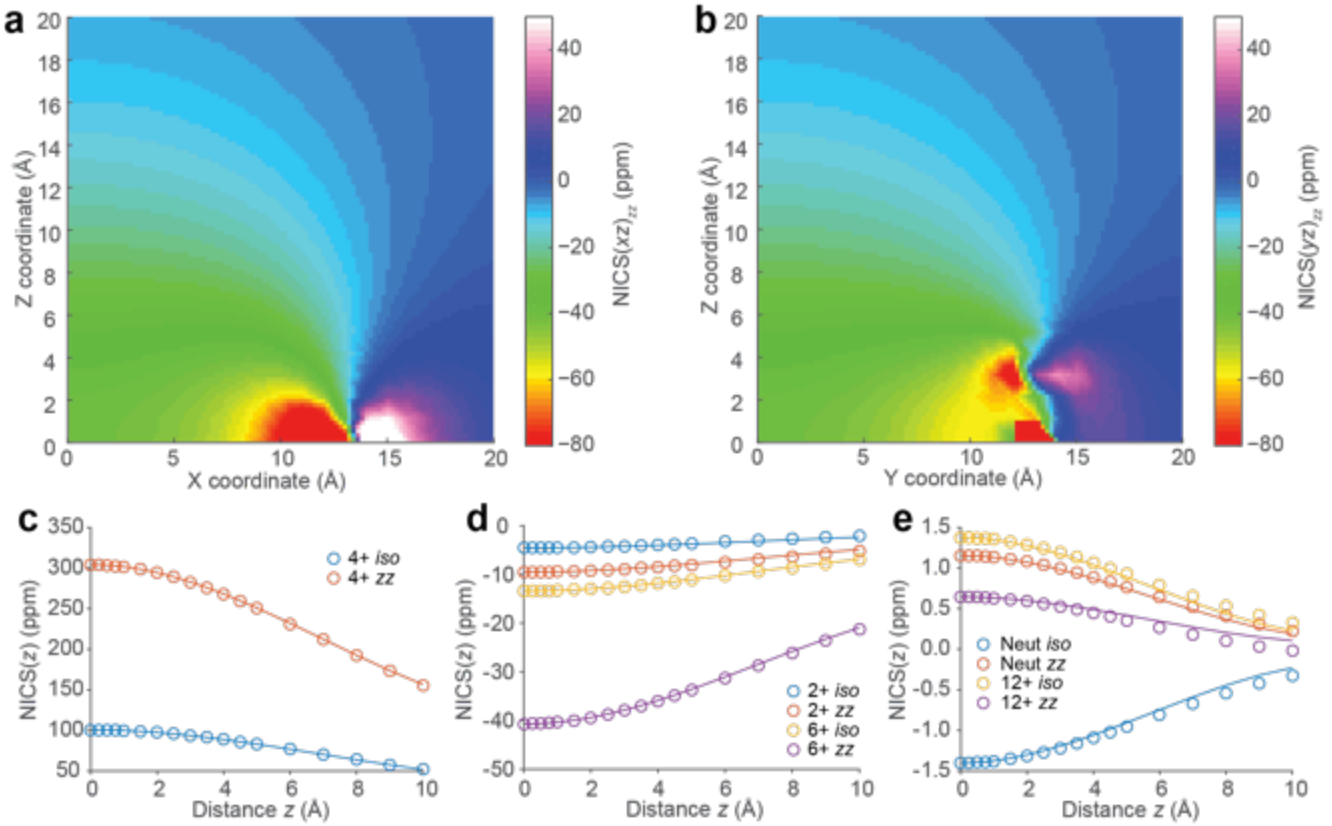

Fig. S7: NICS$_{zz}$ grids for ***c*-P6**$^{6+}$ in (a) the *xz* plane and (b) the *yz* plane of the molecule. In (a), the view bisects a butadiyne and in (b) the view bisects a porphyrin. (c–e) show NICS(*z*) scans along the *z* axis of the molecule (see Figure S6). The fitting lines are described below. Level of theory: B3LYP/6-31G*.

The calculated NICS(*z*) values along the *z* axis of the molecule (Fig. S7 c–e) fit well to a cubic polynomial:

$$\mathrm{NICS}(z) = \frac{\mathrm{NICS}(0)}{100}(az^3 + bz^2 + cz + 100)$$

Where *a*, *b* and *c* are defined by fitting as:

	oxidation states	*a*	*b*	*c*
(Anti)aromatic	2+, 4+, 6+	4.50×10^{-2}	-9.46×10^{-1}	1.10×10^{-1}
Non-aromatic	0, 12+	1.13×10^{-1}	-1.96	-1.30×10^{-1}

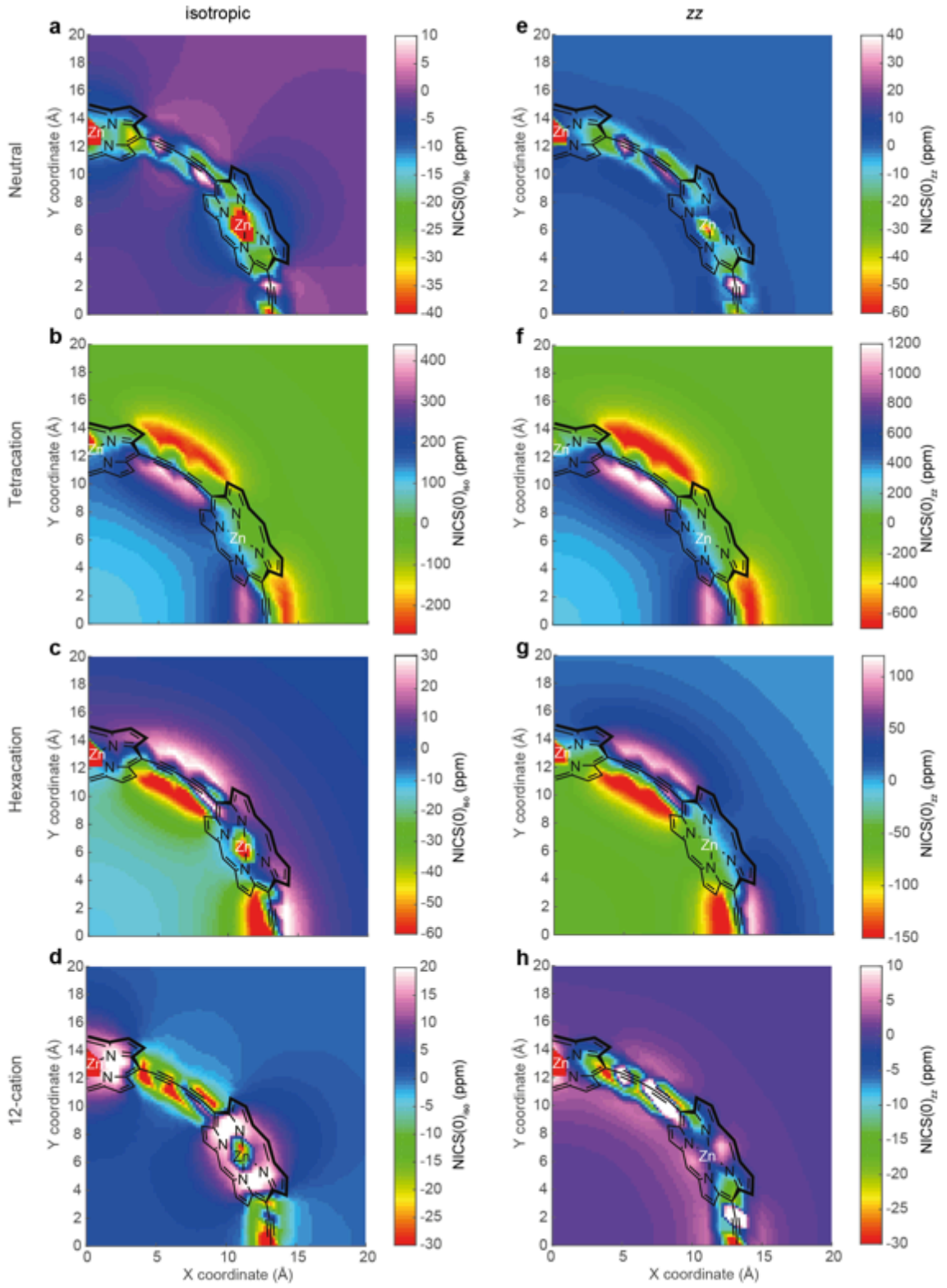

Fig. S8: (a-d) NICS(0)$_{iso}$ grids for neutral, 4+, 6+ and 12+ ***c*-P6**. (e–h): corresponding NICS(0)$_{zz}$ grids. Level of theory B3LYP/6-31G*.

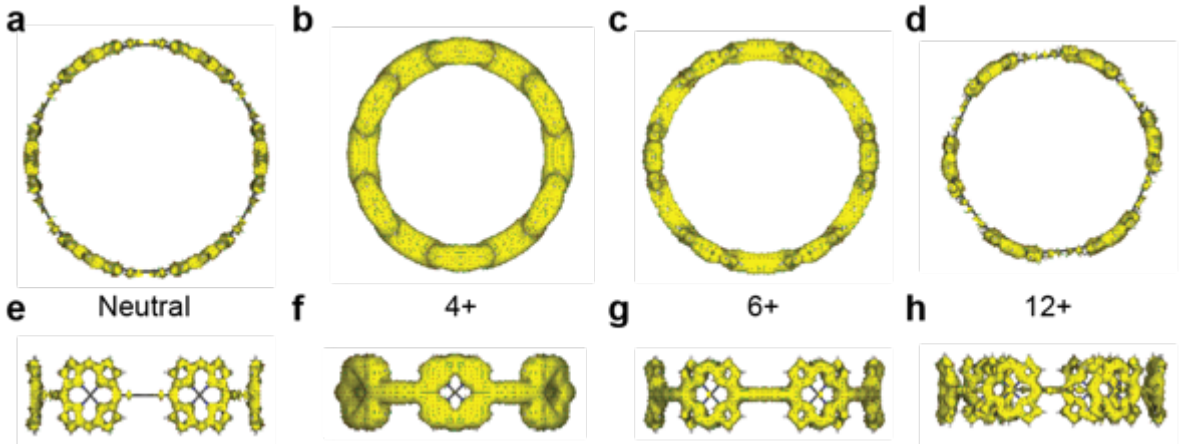

Fig. S9: ACID plots, viewing the molecule along the –*z* axis**,** for an applied magnetic field along the +*z* axis, for (a) ***c*-P6**, (b) ***c*-P6**$^{4+}$ (c) ***c*-P6**$^{6+}$ and (d) ***c*-P6**$^{12+}$. (e–h) show the corresponding views along the *y* axis. The ACID isosurface corresponds to an isovalue of 0.06 a.u.

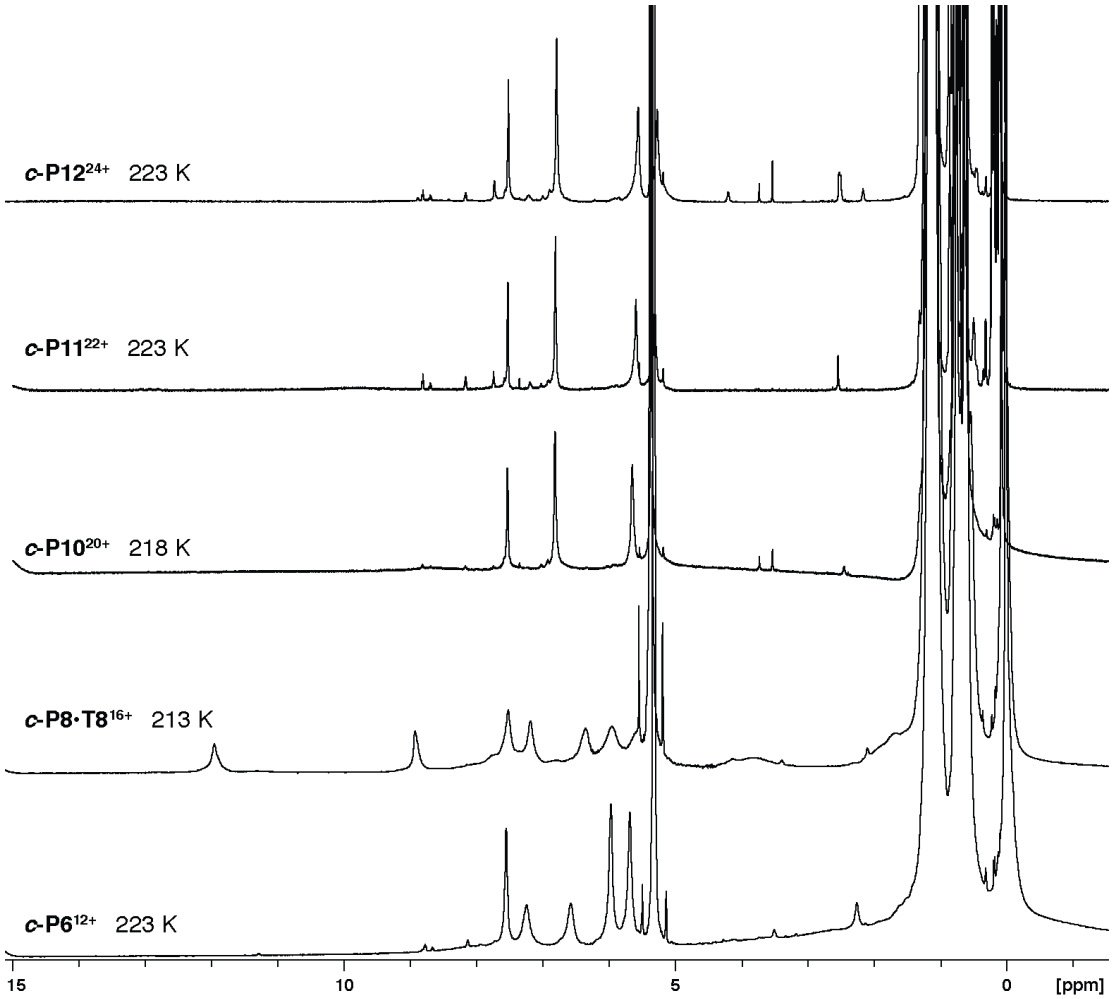

Fig. S10: ^{1}H NMR spectra (500 MHz, CD_2Cl_2) of the 2*N*+ oxidation states of ***c*-P6**, ***c*-P8·T8**, ***c*-P10**, ***c*-P11** and ***c*-P12**, generated by oxidation with excess $DIBAHA_F$.

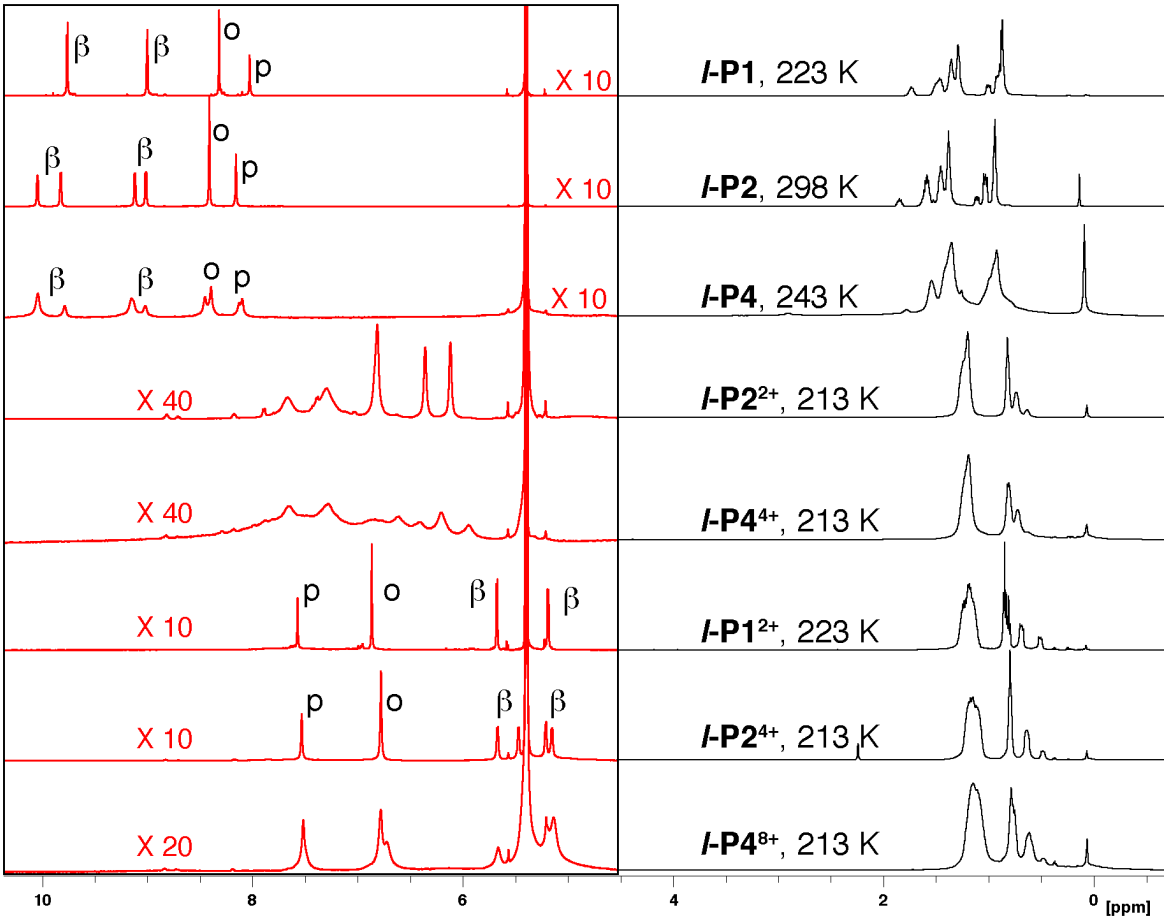

Fig. S11: ^{1}H NMR (500 MHz, CD_2Cl_2) of ***l*-P1**, ***l*-P2** and ***l*-P4** in their diamagnetic neutral, *N*+ and 2*N*+ oxidation states (excluding paramagnetic ***l*-P1**$^{+}$). Labels are described in SI Fig. S5B.

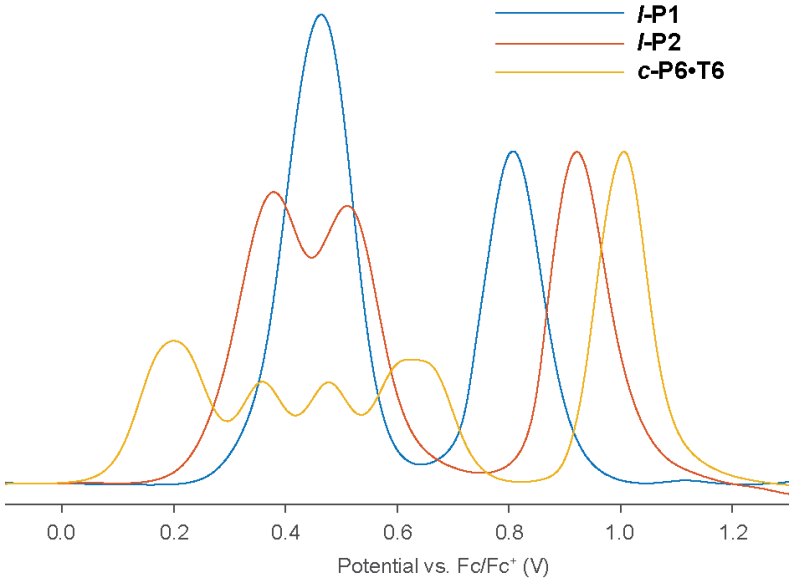

Fig. S12: Square wave voltammetry of ***l*-P1** (blue), ***l*-P2** (red) and ***c*-P6·T6** (orange), in CH_2Cl_2 (0.1 M Bu_4PF_6). The abscissa (current) is normalised to the height of the highest oxidation peak (~ 1 V).

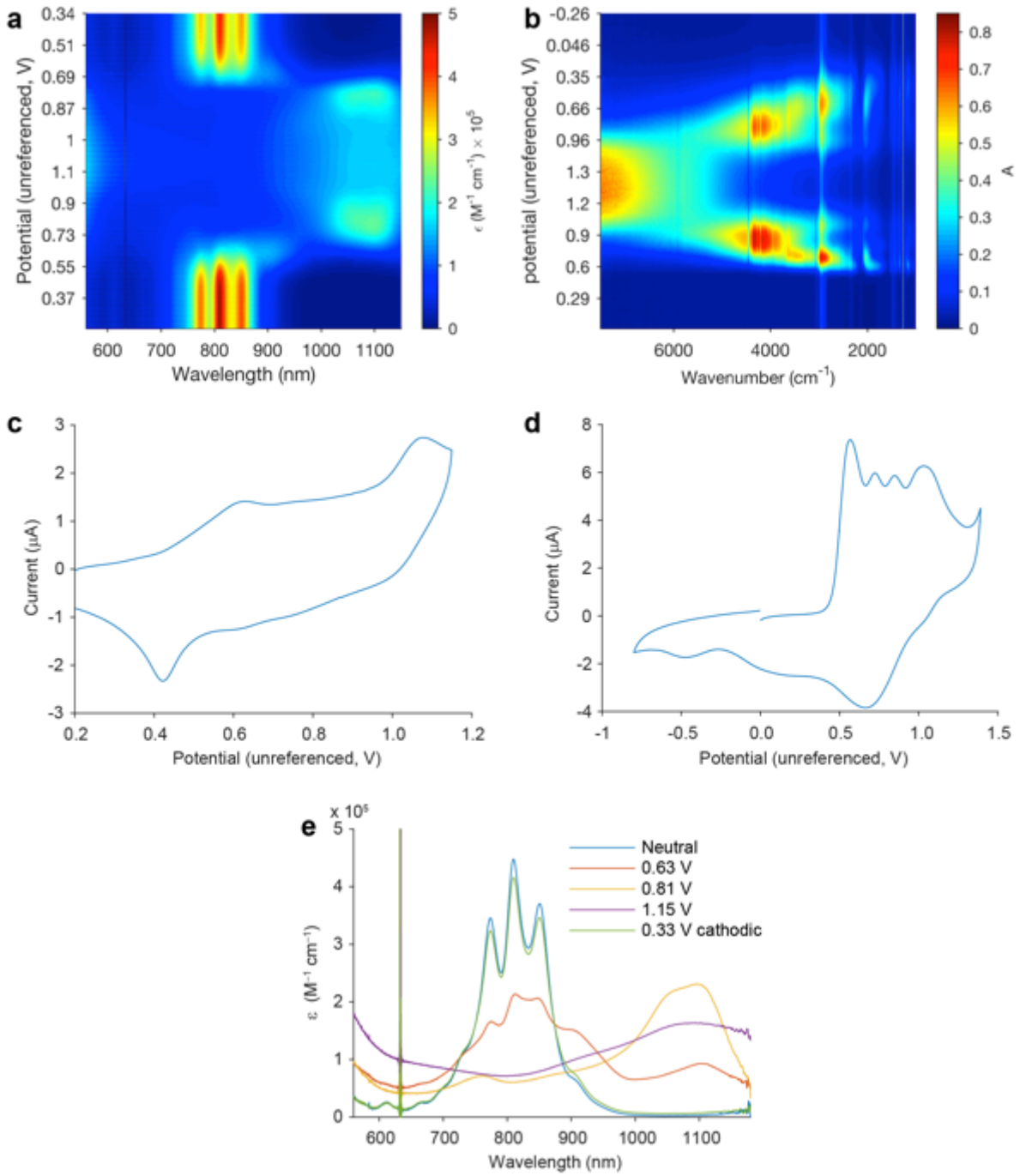

Fig. S13: Thin layer spectroelectrochemistry of ***c*-P6·T6** in CH_2Cl_2 (0.1 M Bu_4NPF_6) in the NIR (a) and IR (b) regions. (c) and (d) show the corresponding cyclic voltammograms to (a) and (b). In part (e), selected spectra corresponding, approximately, to monocation (0.63 V), an intermediate cation (0.81 V) and the hexacation (1.15 V) are presented.

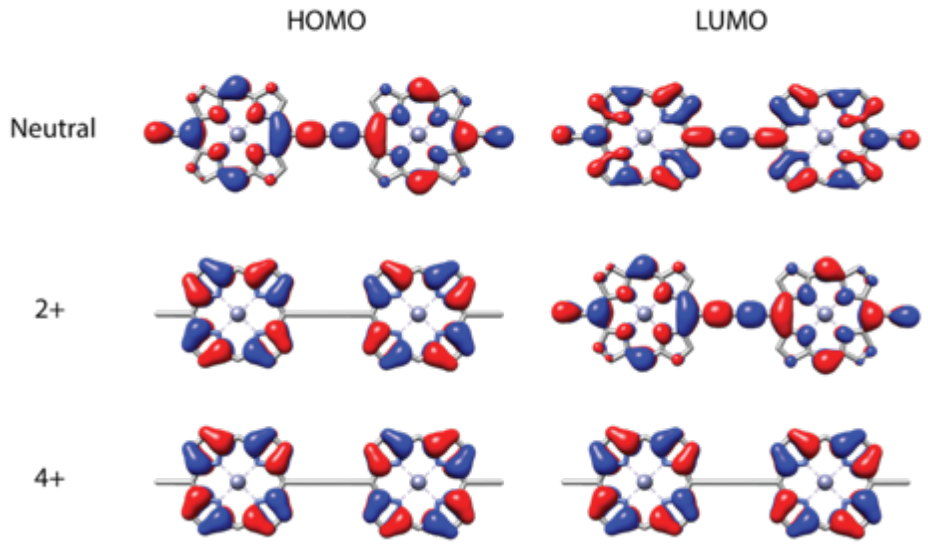

Fig. S14: Frontier orbitals of ***l*-P2** in its neutral, 2+ and 4+ oxidation states. A truncated model of ***l*-P2** was used, with aryl sidegroups and terminal trialkylsilyl alkyne protecting groups truncated to H (overall D_{2h} symmetry). Level of theory: B3LYP/6-31G*.

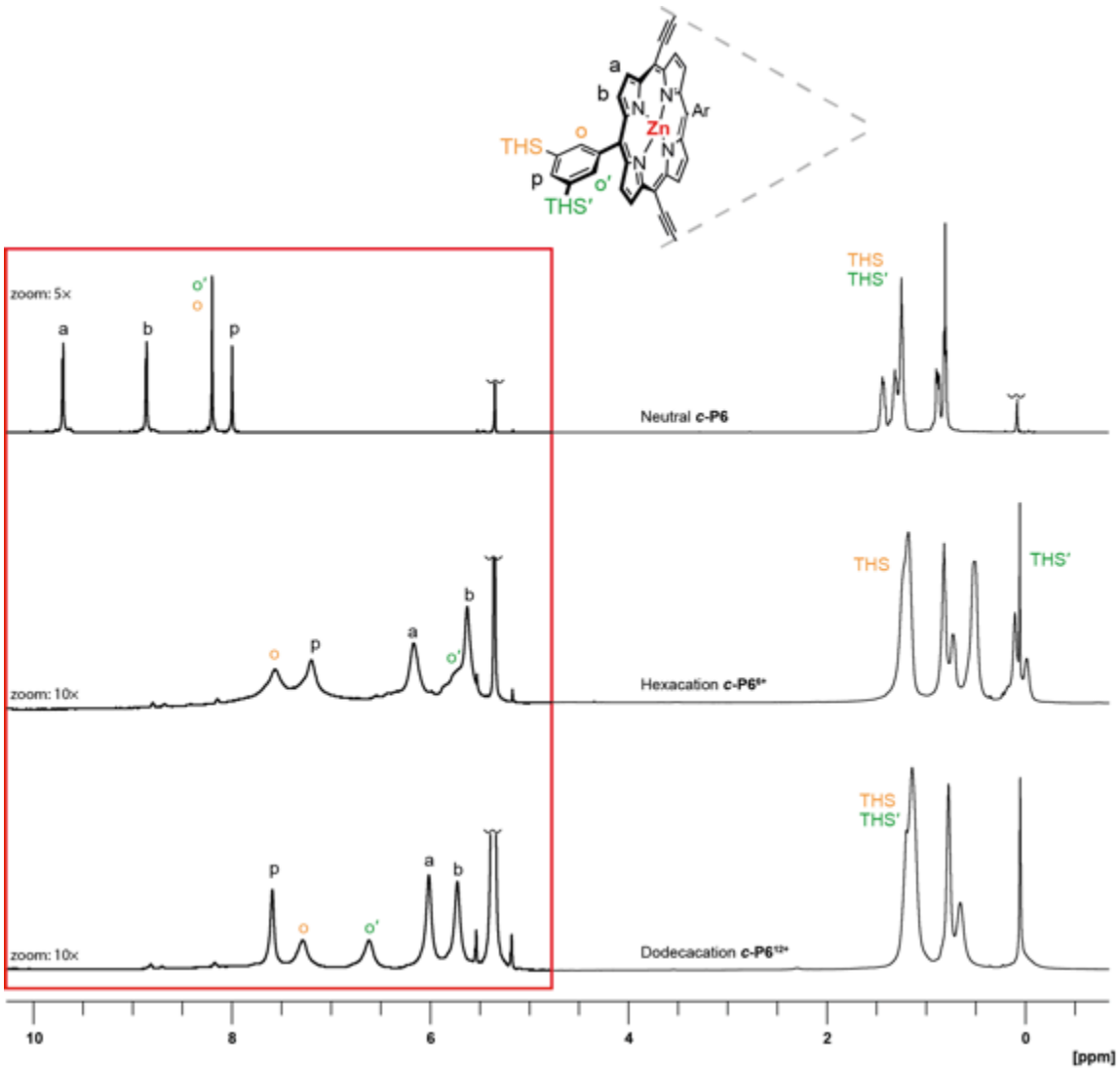

Fig. S15: Comparison of NMR spectra (500 MHz, 223 K, CD_2Cl_2) of template-free ***c*-P6** in its neutral, 6+ and 12+ oxidation states. The 6+ oxidation state was generated by oxidation with excess Thn, and the 12+ oxidation state was generated by oxidation with excess $DIBAHA_F$.

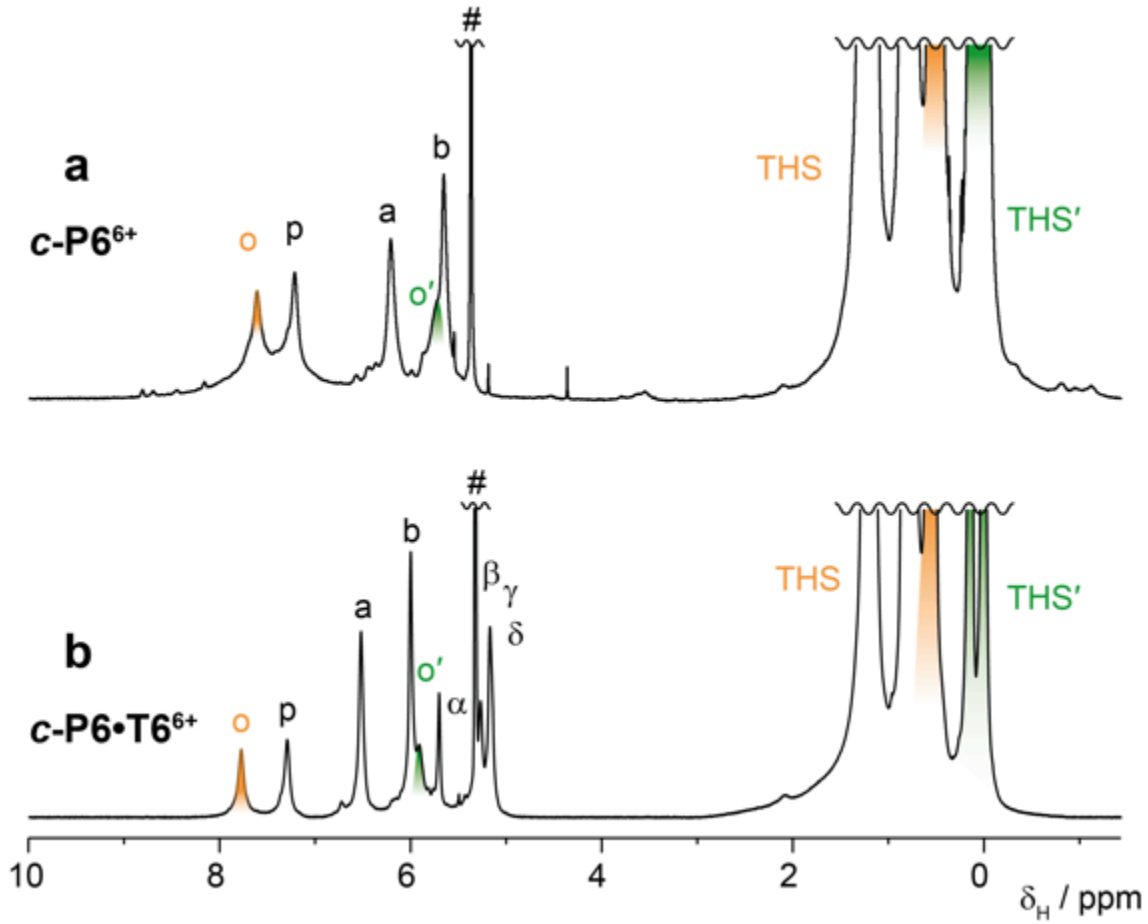

Fig. S16: Comparison of NMR spectra (500 MHz, 223 K, CD_2Cl_2) of ***c*-P6** in its 6+ oxidation state, with (a) and without (b) template. (a) was generated by oxidation with excess Thn; (b) during titration with $AgSbF_6/I_2$.

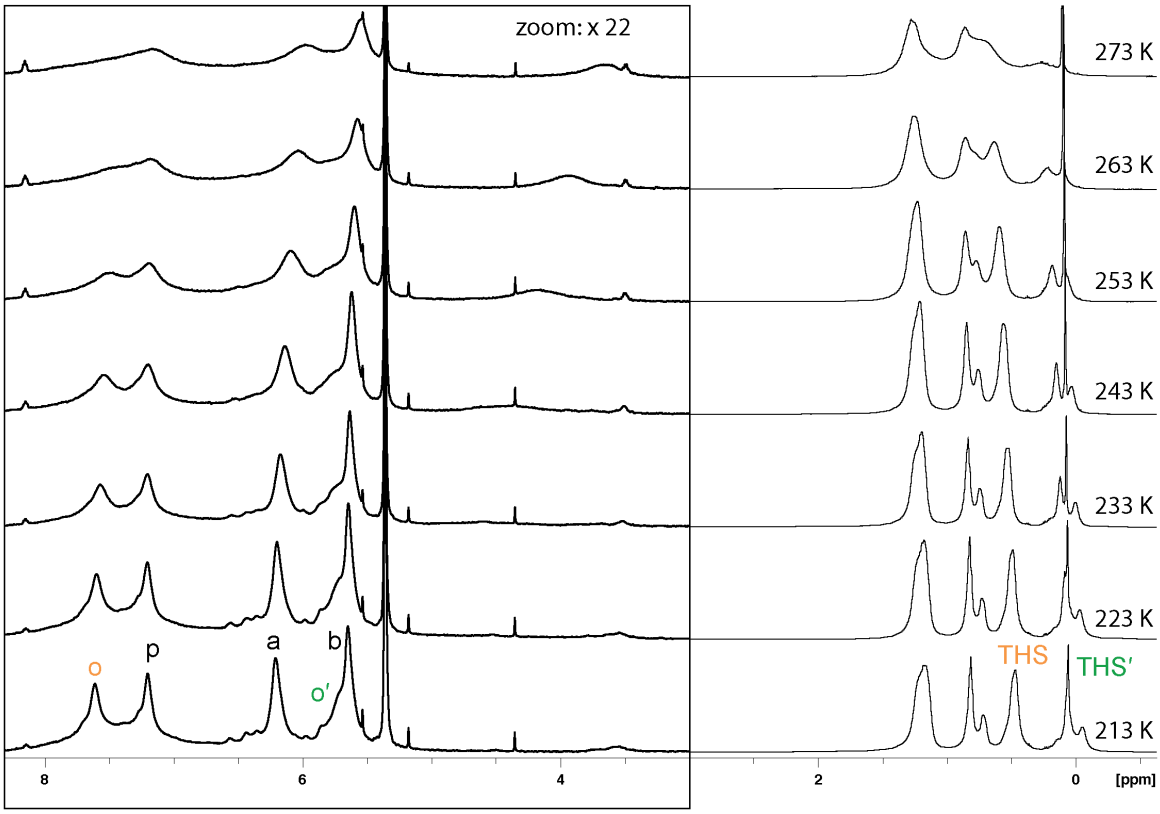

Fig. S17: VT ^{1}H NMR (500 MHz, CD_2Cl_2) of ***c*-P6^{6+}**, generated by oxidation with excess Thn.

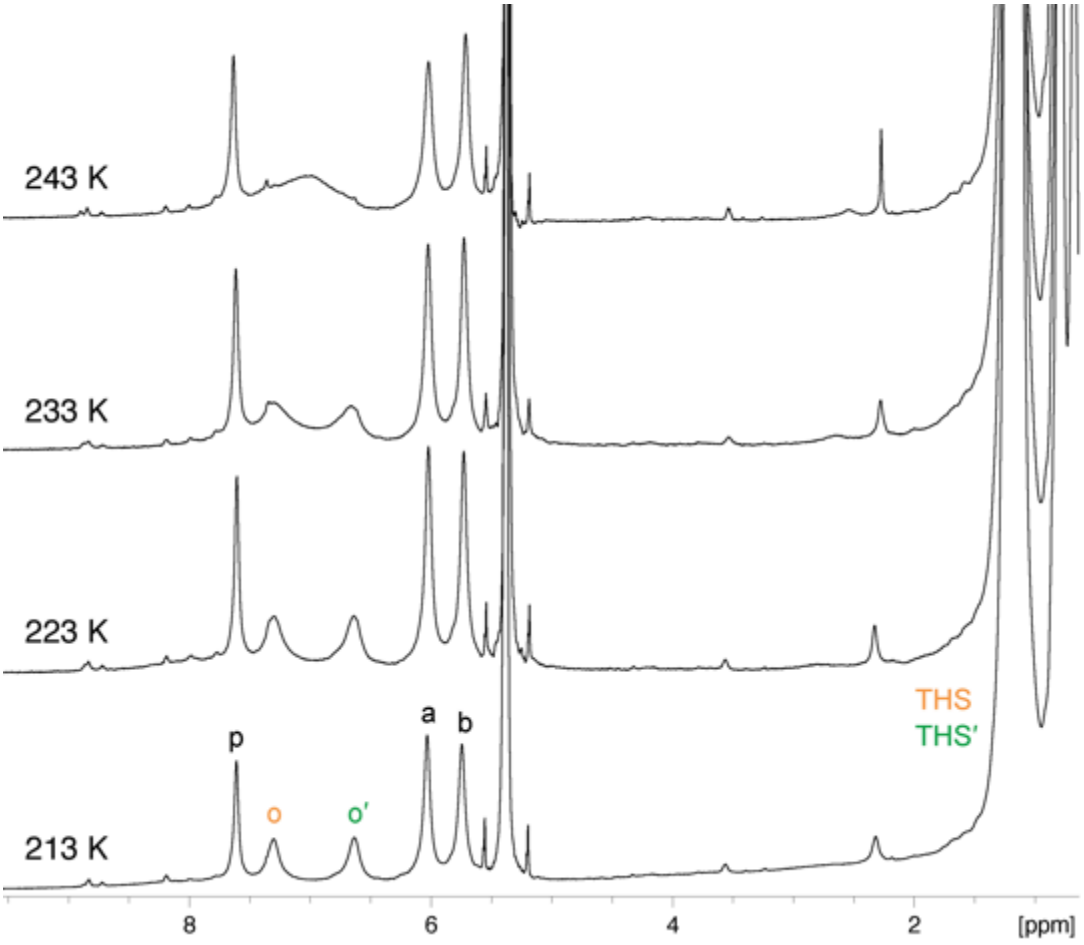

Fig. S18: VT ^{1}H NMR (500 MHz, CD_2Cl_2) of ***c*-P6^{12+}**, generated by oxidation with excess $DIBAHA_F$.

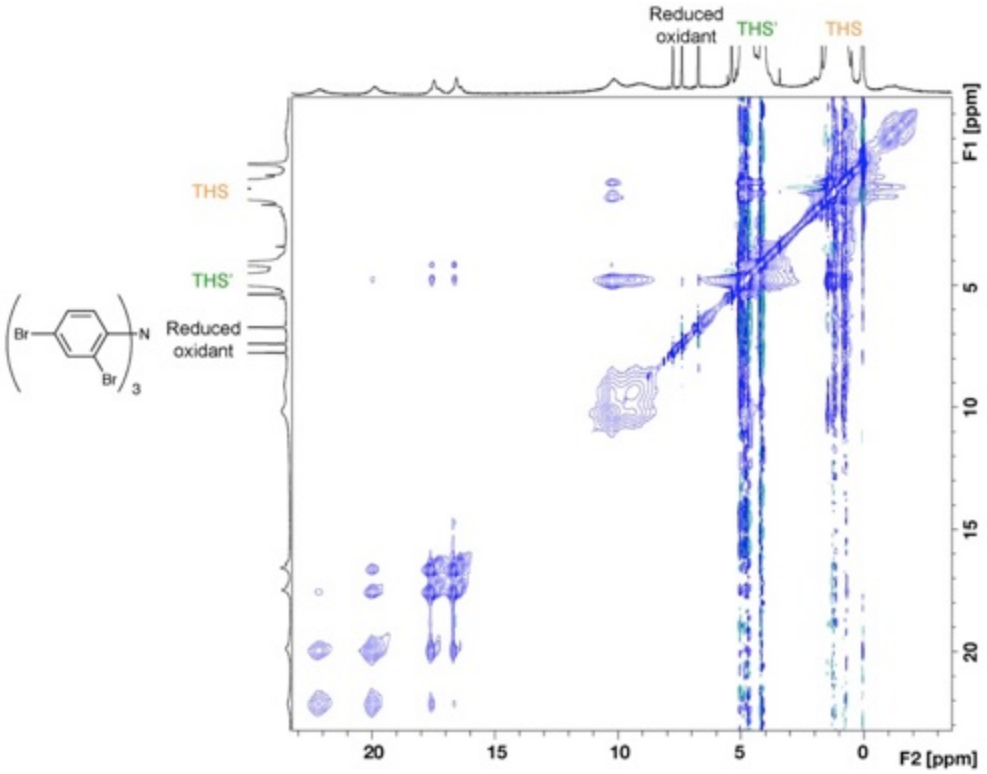

Fig. S19: NOESY of ***c*-P6·T6^{4+}** (500 MHz, 223 K). t_{mix} = 250 ms. This sample was prepared by titration with $DIBAHA_F$.

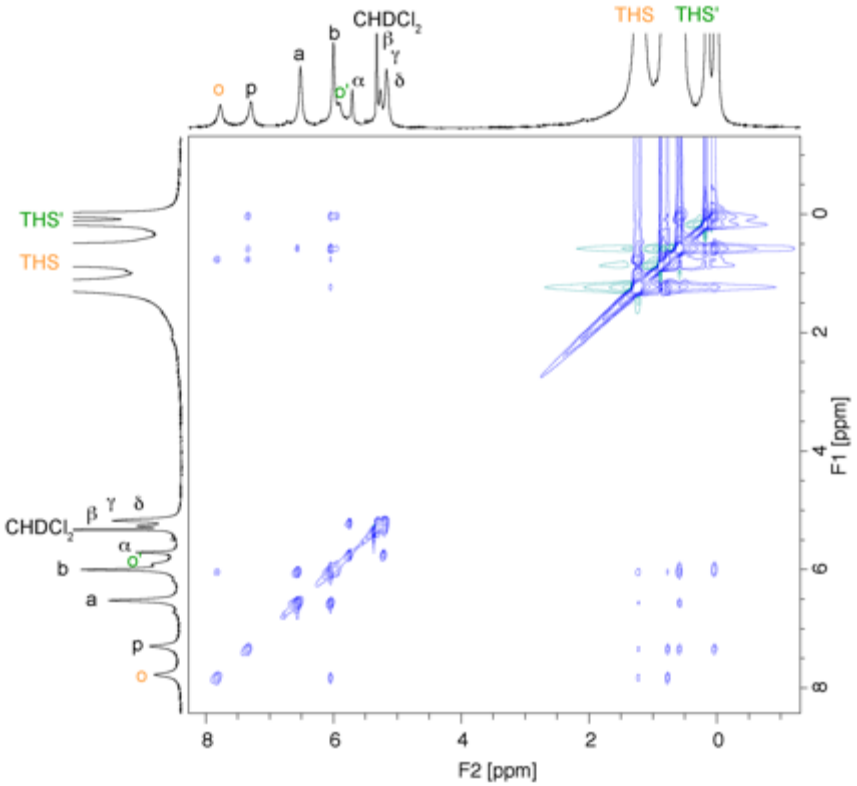

Fig. S20: NOESY of ***c*-P6·T6^{6+}** (500 MHz, 223 K). t_{mix} = 250 ms. This sample was prepared by titration with $AgSbF_6/I_2$.

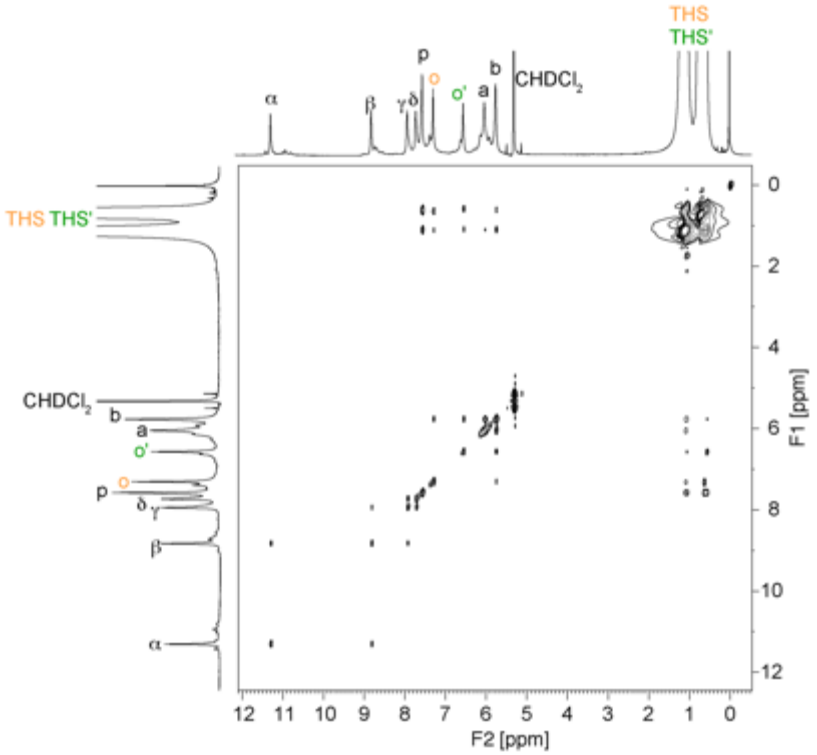

Fig. S21: NOESY of ***c*-P6·T6**$^{12+}$ (500 MHz, 223 K). t_{mix} = 200 ms. This sample was prepared by oxidation with excess $DIBAHA_F$.

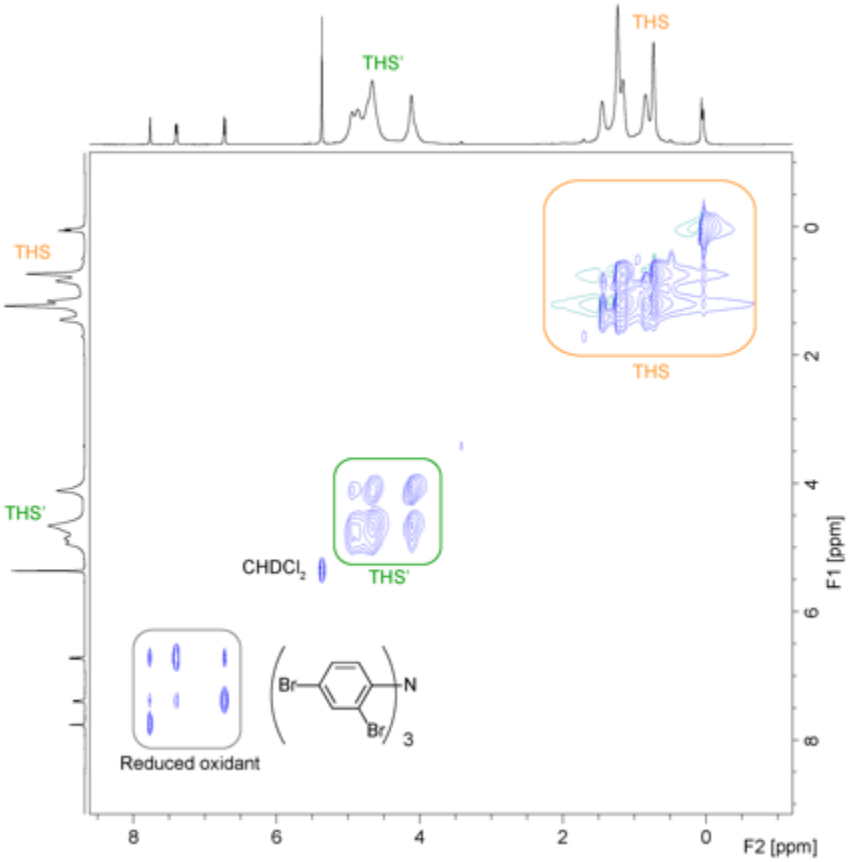

Fig. S22: TOCSY (t_{mix} = 60 ms) of ***c*-P6·T6**$^{4+}$ (500 MHz, 223 K), using the MLEV17 sequence during the TOCSY mixing time. This sample was prepared by titration with $DIBAHA_F$.

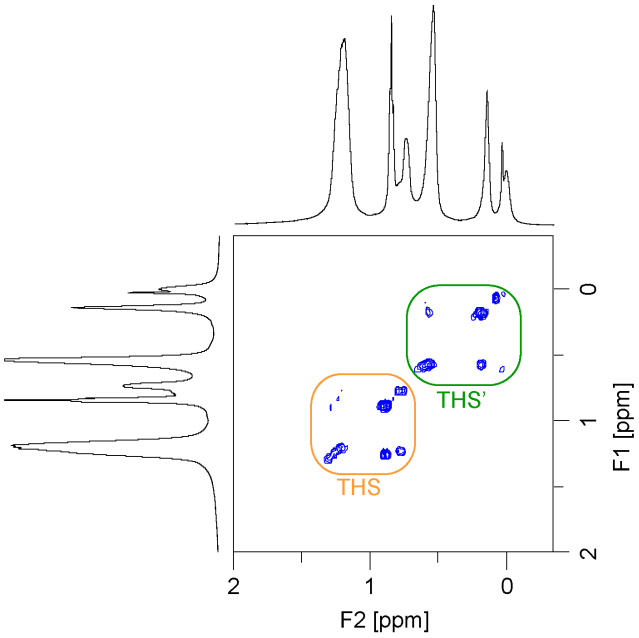

Fig. S23: Expanded COSY of ***c*-P6•T6**$^{6+}$ (500 MHz, 223 K). This sample was prepared by titration with $AgSbF_6/I_2$.

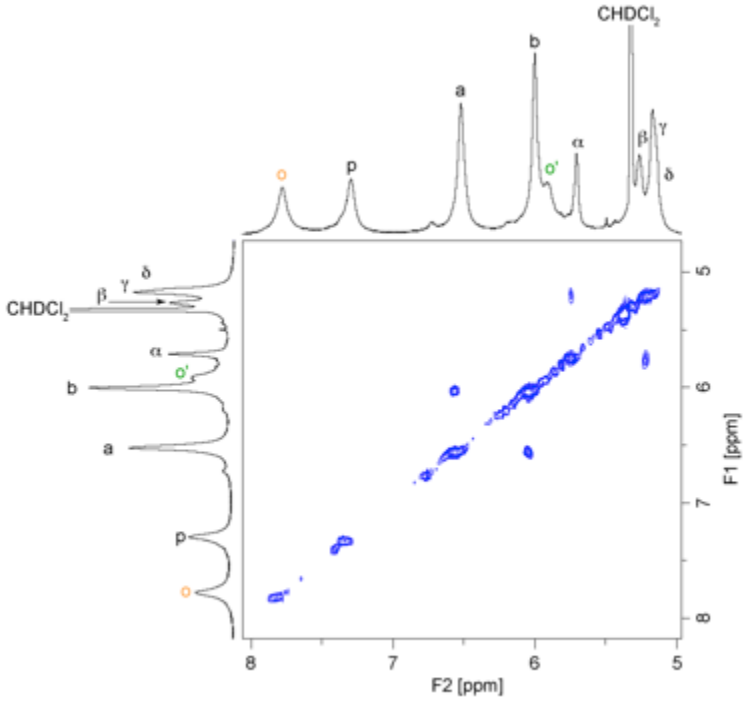

Fig. S24: Expanded COSY of ***c*-P6·T6**$^{6+}$ (500 MHz, 223 K). This sample was prepared by titration with $AgSbF_6/I_2$.

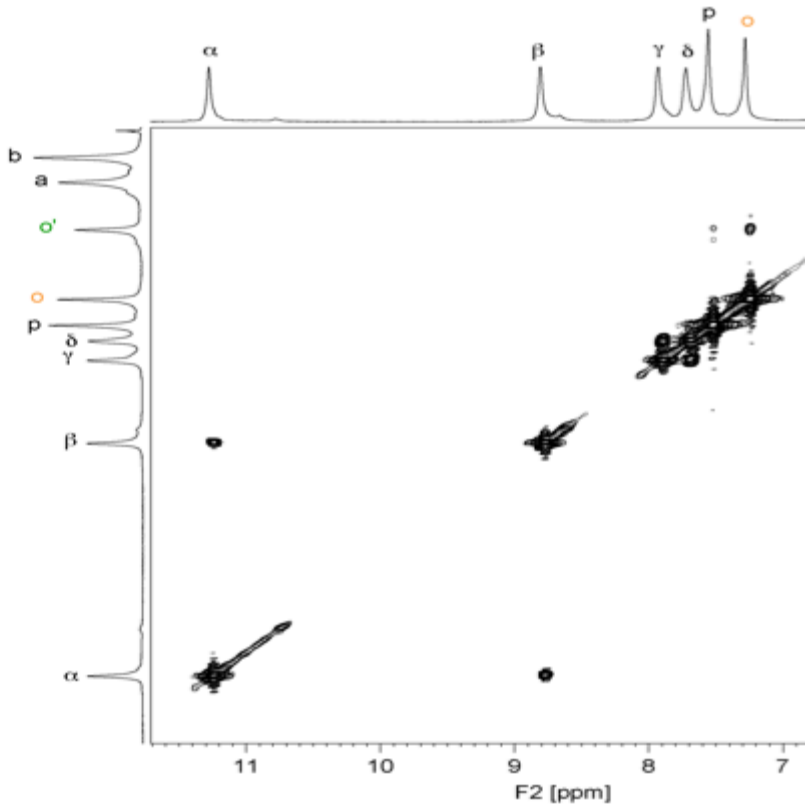

Fig. S25: COSY of ***c*-P6·T6**$^{12+}$ (500 MHz, 213 K). This sample was prepared by oxidation with excess $DIBAHA_F$.

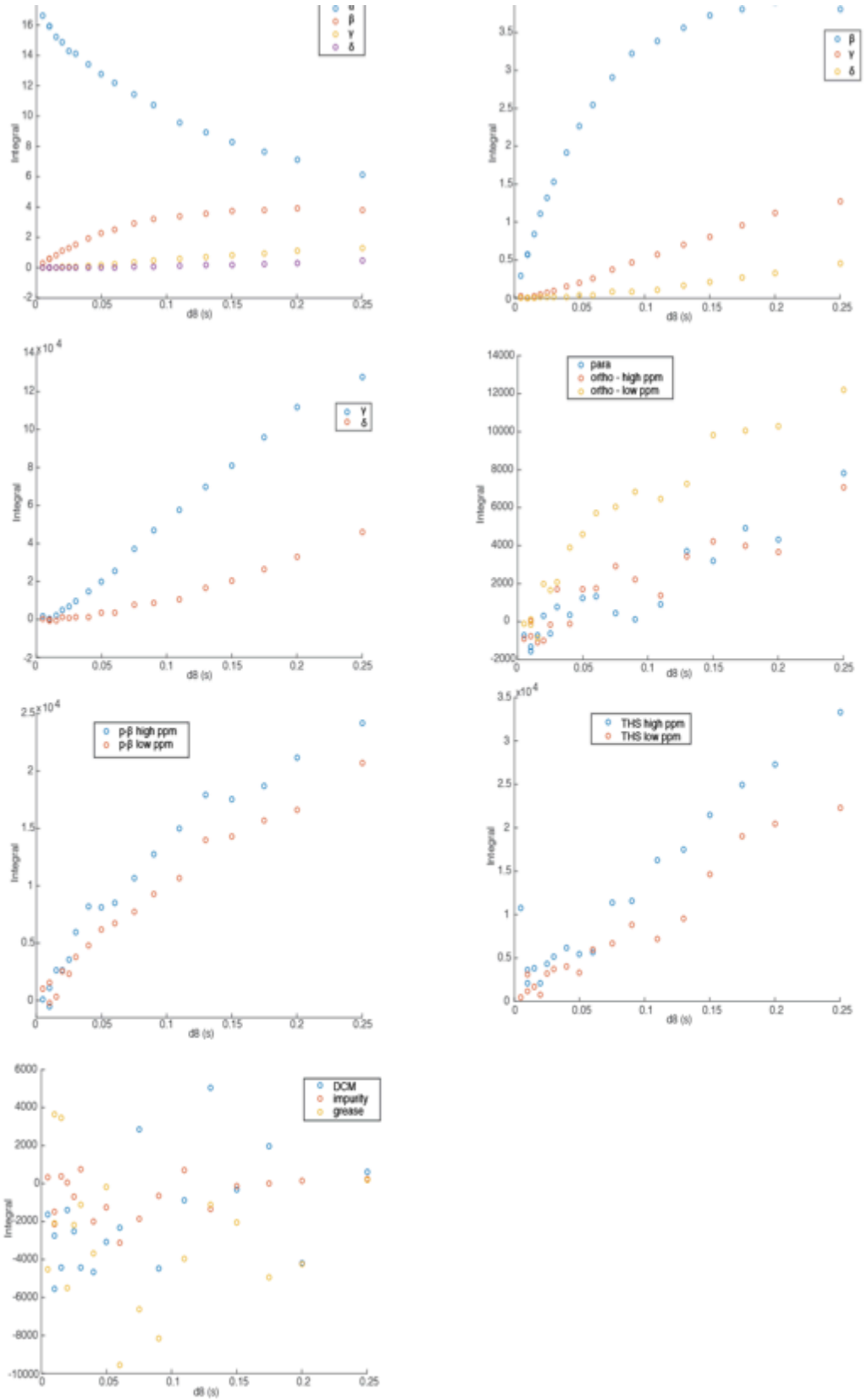

Fig. S26: Transient ^{1}H NOE (500 MHz, CD_2Cl_2, 223 K) buildup/decay curves for ***c*-P6·T6**$^{12+}$, with NOE transfer following selective excitation (t_{mix} = *d8*) of the template α proton. The sample was prepared by oxidation with excess $DIBAHA_F$.

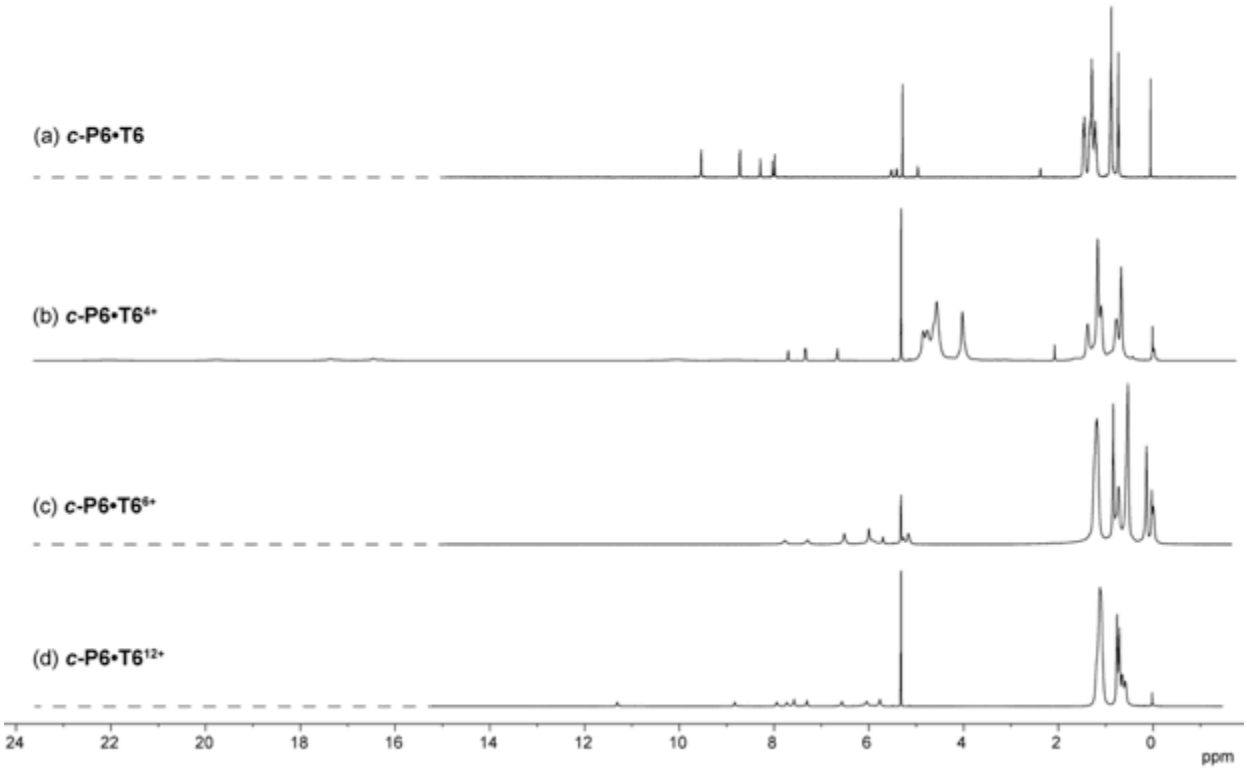

Fig. S27: Full ^{1}H NMR spectra (500 MHz) of (a) neutral ***c*-P6·T6** (298 K); (b) ***c*-P6·T6^{4+}** generated during titration with $DIBAHA_F$, 223 K; (c) ***c*-P6·T6^{6+}** generated during titration with $AgSbF_6/I_2$, 223 K; (d) ***c*-P6·T6^{12+}** generated by oxidation with excess $DIBAHA_F$, 223 K. (*cf.* expanded extract in Fig. 4, main text).

References

S1. C. E. Tait, P. Neuhaus, M. D. Peeks, H. L. Anderson, C. R. Timmel, Transient EPR reveals triplet state delocalization in a series of cyclic and linear π-conjugated porphyrin oligomers. *J. Am. Chem. Soc.* **137**, 8284–8293 (2015).

S2. N. G. Connelly, W. E. Geiger, Chemical redox agents for organometallic chemistry. *Chem. Rev.* **96**, 877–910 (1996).

S3. M. J. Frisch *et al.*, Gaussian 09 Revision D.01, Gaussian Inc. Wallingford CT (2009).

S4. A. D. Becke, Density-functional thermochemistry. III. The role of exact exchange. *J. Chem. Phys.* **98**, 5648–5652 (1993).

S5. W. J. Hehre, R. Ditchfield, J. A. Pople, Self-consistent molecular orbital methods. XII. Further extensions of Gaussian-type basis sets for use in molecular orbital studies of organic molecules. *J. Chem. Phys.* **56**, 2257–2261 (1972).

S6. V. A. Rassolov, J. A. Pople, M. A. Ratner, T. L. Windus, 6-31G* basis set for atoms K through Zn. *J. Chem. Phys.* **109**, 1223–1229 (1998).

S7. D. Geuenich, K. Hess, F. Kohler, R. Herges, Anisotropy of the induced current density (ACID), a general method to quantify and visualize electronic delocalization. *Chem. Rev.* **105**, 3758–3772 (2005).

S8. S. Grimme, J. Antony, S. Ehrlich, H. Krieg, A consistent and accurate ab initio parameterization of density functional dispersion correction (DFT-D) for the 94 elements H-Pu. *J. Chem. Phys.* **132**, 154104 (2010).

S9. Y. Zhao, D. G. Truhlar, The M06 suite of density functionals for main group thermochemistry, thermochemical kinetics, noncovalent interactions, excited states and transition elements: two new functionals and systematic testing of four M06-class functionals and 12 other functionals. *Theor. Chem. Acc.* **120**, 215–241 (2008).

S10. J.-D. Chai, M. Head-Gordon, Long-range corrected hybrid density functionals with damped atom-atom dispersion corrections. *Phys. Chem. Chem. Phys.* **10**, 6615–6620 (2008).

S11. M. D. Peeks, P. Neuhaus, H. L. Anderson, Experimental and computational evaluation of the barrier to torsional rotation in a butadiyne-linked porphyrin dimer. *Phys. Chem. Chem. Phys.* **18**, 5264–5274 (2016).

S12. J. Jeener, B. H. Meier, P. Bachmann, R. R. Ernst, Investigation of exchange processes by two-dimensional NMR spectroscopy. *J. Chem. Phys.* **71**, 4546–4549 (1979).

S13. C. L. Perrin, T. J. Dwyer, Application of two-dimensional NMR to kinetics of chemical exchange. *Chem. Rev.* **90**, 935–967 (1990).

S14. M. L. H. Green, L. L. Wong, A. Sella, Relationship between intramolecular chemical exchange and NMR-observed rate constants. *Organometallics*. **11**, 2660–2668 (1992).

S15. S. Liu *et al.*, Caterpillar track complexes in template-directed synthesis and correlated molecular motion. *Angew. Chem. Int. Ed.* **54**, 5355–5359 (2015).

S16. D. F. Evans, 400. The determination of the paramagnetic susceptibility of substances in solution by nuclear magnetic resonance. *J. Chem. Soc.* 2003–2005 (1959).

S17. E. M. Schubert, Utilizing the Evans method with a superconducting NMR spectrometer in the undergraduate laboratory. *J. Chem. Educ.* **69**, 62 (1992).

S18. D. H. Grant, Paramagnetic susceptibility by NMR. *J. Chem. Educ.* **72**, 39–40 (1995).

S19. C. Piguet, Paramagnetic susceptibility by NMR: the "solvent correction" removed for large paramagnetic molecules. *J. Chem. Educ.* **74**, 815–816 (1997).